Nuclear Engineering and Design 448 (2026) 114735

Contents lists available at ScienceDirect

Nuclear Engineering and Design

journal homepage: www.elsevier.com/locate/nucengdes

# Experimental investigations of Pool hydrodynamics and aerosol removal under low momentum injection

Nabil Ghendour [a,*], Detlef Suckow [a], Abdelouahab Dehbi [a], Michael Klauck [b]

[a] Paul Scherrer Institut (PSI), Forschungsstrasse 111, 5232 Villigen PSI, Switzerland
[b] Forschungszentrum Jülich GmbH (FZJ), 52425 Jülich, Germany

ARTICLE INFO

*Keywords:*
FCVS
Pool scrubbing
Globule regime
Bubble hydrodynamics
Aerosol retention
Wire mesh sensor
High-speed camera

ABSTRACT

A detailed experimental database was generated from hydrodynamic characterization a Wire Mesh Sensor (WMS) and a High-Speed Camera (HSC) in the TRISTAN facility and aerosol retention measurements in the SAAB facility, performed under identical injection conditions in the low-momentum globule regime. Nitrogen was injected through 5 mm and 10 mm nozzles, spanning a flow range of 1–10 $l_n$/min, with a water submergence of 300 mm. This corresponds to a Weber number up to 7.3. HSC images showed aperiodic globule formation, revealing intensified bubble coalescence and break-up with increasing flow rates. The image processing demonstrated a high Gas Void Fraction (GVF) in the injection region, which increases with flow rate. The WMS data were collected at heights of 40, 100, and 200 mm above the nozzle tip. The data analysis mirrored GVF trends from the HSC images. Furthermore, the velocity profile of the gas phase was analyzed. Notably, the impact of the nozzle diameter is prominent in the injection region near the nozzle. An advanced algorithm was developed to track and extract globule formation characteristics from HSC images. A new scaling concept to describe globule characteristics as function of the Weber number was introduced and validated using additional experimental data. Based on this, a new correlation for the globule diameter is proposed for Weber number up to 70. Corresponding aerosol pool scrubbing tests were conducted and showed that particle retention is roughly insensitive to the gas flow rate within the experimental range, but is enhanced as particle inertia increases. In addition, use of the smaller nozzle under similar flow rates results mostly in a slight improvement of aerosol removal. These high-fidelity data can serve to develop and validate CFD models for hydrodynamics and aerosol pool scrubbing.

## 1. Introduction

The escalating concerns about environmental pollution and carbon emissions have intensified global efforts toward clean energy alternatives. Nuclear energy stands out as a promising solution to address the challenges posed by fossil fuels (Zhang et al., 2022a). This justifies the notable increase in the number of nuclear power plants across the globe in recent decades. Despite the low probability of accidents in NPPs, safety was and remains the main concern in their design and operation. For instance, in the case of a core meltdown accident, the release of radioactive Fission Products (FP) would have severe implications for both human life and the environment. Hence, extensive research has been conducted and several safety systems have been developed to prevent, reduce, and stop the leakage of the FP in such scenarios.

Wet-scrubber Filtered Containment Venting Systems (FCVS) are widely used as the last protection stage to avoid overpressure failure of the containment in case of reactor pressure vessel failure. This system consists of a vessel filled with water, in which the contaminated gas is injected to decrease atmospheric pressure in the containment. By bubbling the contaminated gas in the water pool, as shown in Fig. 1, a large fraction of radioactive FP can be scrubbed (Kim et al., 2020). Such systems are widely used in the world due to their high efficiency in FP retention (Dong and Yang, 2019).

Understanding the release, transport, and retention mechanisms of these FP is pivotal to accurately quantify the potential radioactivity that could be released into the environment (Dehbi et al., 2001; Diao et al., 2020). Over the past few decades, extensive research has led to the development of models and correlations that are widely employed to calculate FP retention under diverse conditions. However, due to the often complex dynamics involved, these models necessitate numerous

* Corresponding author.
*E-mail address:* nabil.ghendour@psi.ch (N. Ghendour).

https://doi.org/10.1016/j.nucengdes.2025.114735
Received 20 September 2025; Received in revised form 22 December 2025; Accepted 27 December 2025
Available online 2 January 2026

assumptions and simplifications, consequently introducing significant uncertainties into the results (Roth et al., 2022). The advent and progress of Computational Fluid Dynamics (CFD) provide a promising avenue for developing new, more accurate models for low momentum injection conditions. However, the main challenge is the availability of CFD-grade validation data.

Considerable experimental research work has been directed toward understanding the behavior and dynamics of bubble formation of submerged nozzles. A significant portion of these studies has concentrated on the dynamics within the single bubbling regime (Fujiwara et al., 2019; Liu et al., 2015; Pan et al., 2020; Wang et al., 2024). In this regime, bubbles are formed periodically and flow without any interaction with the other bubbles. Furthermore, numerous CFD assessments were performed to study the internal dynamic of single bubbles rising in a pool. For instance, (Dehbi et al., 2022) provide a CFD comparative exercise of single globule regime simulation using different codes (CFX, Fluent, Star-CCM+, OpenFOAM) and employing both the Euler-Euler and Interface Tracking methodologies. In (Pan et al., 2020), a CFD assessment was carried out to study the effect of the deformation of one rising bubble on particle retention. The dependency of the latter on the bubble wake region was numerically examined in (Zhang et al., 2022b).

Overall, the validation of CFD models for the periodic globule regime primarily involves comparing bubble characteristics (diameter and rise velocity), globule frequency, gas void fraction, and velocity profiles. However, at higher gas flow rates, interactions occur among the generated globules, including coalescence and break-up, leading to chaotic flow behavior. This complexity poses challenges for the accurate measurement and tracking of the bubbles in this regime.

Numerous experimental studies have delved into the aperiodic globule regime, employing various measurement techniques. For example, in (Hur et al., 2013), bubble formation through an orifice in a rectangular bubble column was investigated using a high-speed camera. This study emphasized events such as wake effects and orifice-induced turbulent flow, highlighting the detachment period as a crucial indicator of bubble formation steps, significantly influenced by diverse events. Another study, (Mosdorf and Wyszkowski, 2011), utilized pressure and laser phototransistor sensors alongside HSC recordings to characterize generated globules for different flow ranges. In (Abe et al., 2018), the gas void fraction and velocity distributions over the cross-section were analyzed using a wire mesh sensor for a 6 mm nozzle diameter, examining the impact of flow rate at different heights along the test section. Furthermore, in (Farhat et al., 2021), comprehensive qualitative descriptions of various sub-patterns observed within aperiodic regimes and bubble-bubble interactions were provided through images captured by the HSC. In contrast to the periodic globule regime, there is a lack of quantitative data for the aperiodic regime, especially across varying parameters.

In this work, an extensive experimental investigation was carried out to study bubble hydrodynamics and aerosol retention from a submerged nozzle in a shallow pool, using the TRISTAN and SAAB facilities, respectively. High-speed camera and wire-mesh sensor were used to characterize the multiphase flow, while membrane filter sampling was employed for aerosol retention analysis. A particular focus was placed on globule formation dynamics, with the development of an advanced image-processing algorithm and a scaling approach based on the Weber number. The study aims to provide a comprehensive database and propose generalized correlations for globule properties, supporting future validation of CFD models and improved understanding of retention mechanisms at low injection flow conditions.

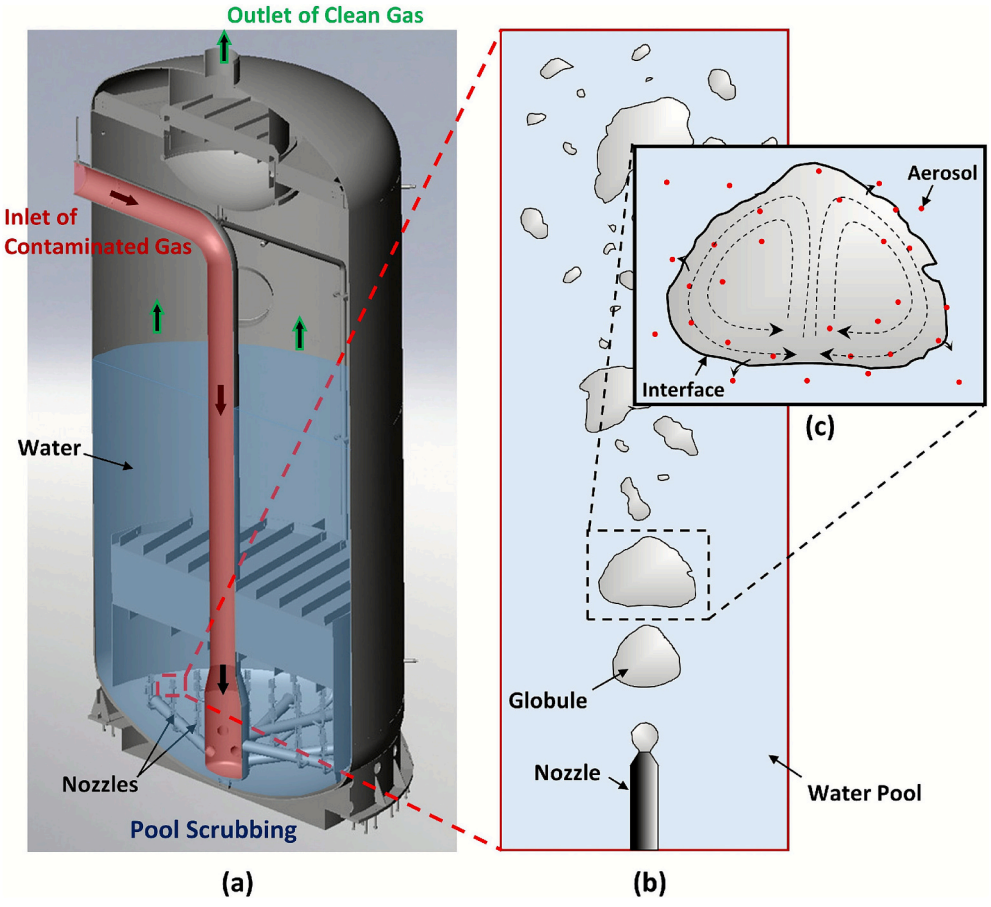


**Fig. 1.** Aerosol retention in wet-scrubber FCVS, (a) wet-scrubber FCVS design, (b) Zoom at the injection region, (c) Aerosol removal process.

## 2. Experimental details

The main objective of this work is to provide well-controlled hydrodynamics and aerosol retention data in the globule regime for CFD code validation. Achieving this objective requires, on the one hand, detailed hydrodynamics characterization of the flow and, on the other hand, reliable generation and measurement of aerosols under well-defined conditions. These requirements could not be fully met within a single experimental facility at our disposal. Therefore, the experiments were conducted in two separate but complementary facilities: TRISTAN and SAAB. The TRISTAN facility is specifically designed and extensively instrumented for high-resolution hydrodynamics measurements. In contrast, the SAAB facility is equipped with dedicated systems for aerosol generation, injection, and measurement, which are essential for quantifying aerosol retention. To ensure consistency and comparability of the data, the experiments in both facilities were performed under identical test conditions, including geometry, flow regime, and operating parameters. This approach allows the hydrodynamics data obtained in TRISTAN to be directly linked to the aerosol retention measurements performed in SAAB, providing a coherent and comprehensive experimental database for CFD validation.

### 2.1. TRISTAN facility – Hydrodynamics experiments

The experiments were conducted in the TRISTAN facility (Fig. 2) at the Paul Scherrer Institut (PSI). The test section has a square cross-section of 50 × 50 $cm^2$ and a total height of 6.106 m. The lower part is equipped with acrylic windows for flow visualization and High-Speed Camera (HSC) recordings, while the upper part is made entirely of stainless steel. Two large Wire Mesh Sensors (WMS) are installed between the two sections. The facility was filled with demineralized water to a level 300 mm above the nozzle tip. The volume below the nozzle is sufficient to allow water recirculation. Pure nitrogen was injected through the nozzles, regulated by a Brooks mass flow controller with an accuracy of ±1 % of full scale.

The HSC and WMS experiments were performed in TRISTAN at two different elevations, as shown in Fig. 3(a). At level A, the nozzle was mounted using 12 mm outer diameter pipes arranged in a U-shape. For the WMS measurements, performed at approximately 3.5 m above ground level (Level B), an L-shaped pipe was used to hold the nozzle, as illustrated in Fig. 3(b). Adjusting the distance between the nozzle and WMS was achieved by changing the connecting pipe. Three Nozzle-WMS distances were selected: 40, 100, and 200 mm. The closest distance was set at 40 mm to prevent potential damage to the WMS, while the maximum distance was set at 200 mm to avoid any impact from water surface instability during the experiments.

#### 2.1.1. Measurement

*2.1.1.1. High speed camera.* A LaVision High-Speed Star HSS 5.1 high-speed camera is installed next to the test section for flow recording. The HSC is equipped with a Nikon Nikkor 28–105 mm lens and adjustable elevation to adjust the field of view inside the channel and capture the region of interest according to the experiment's

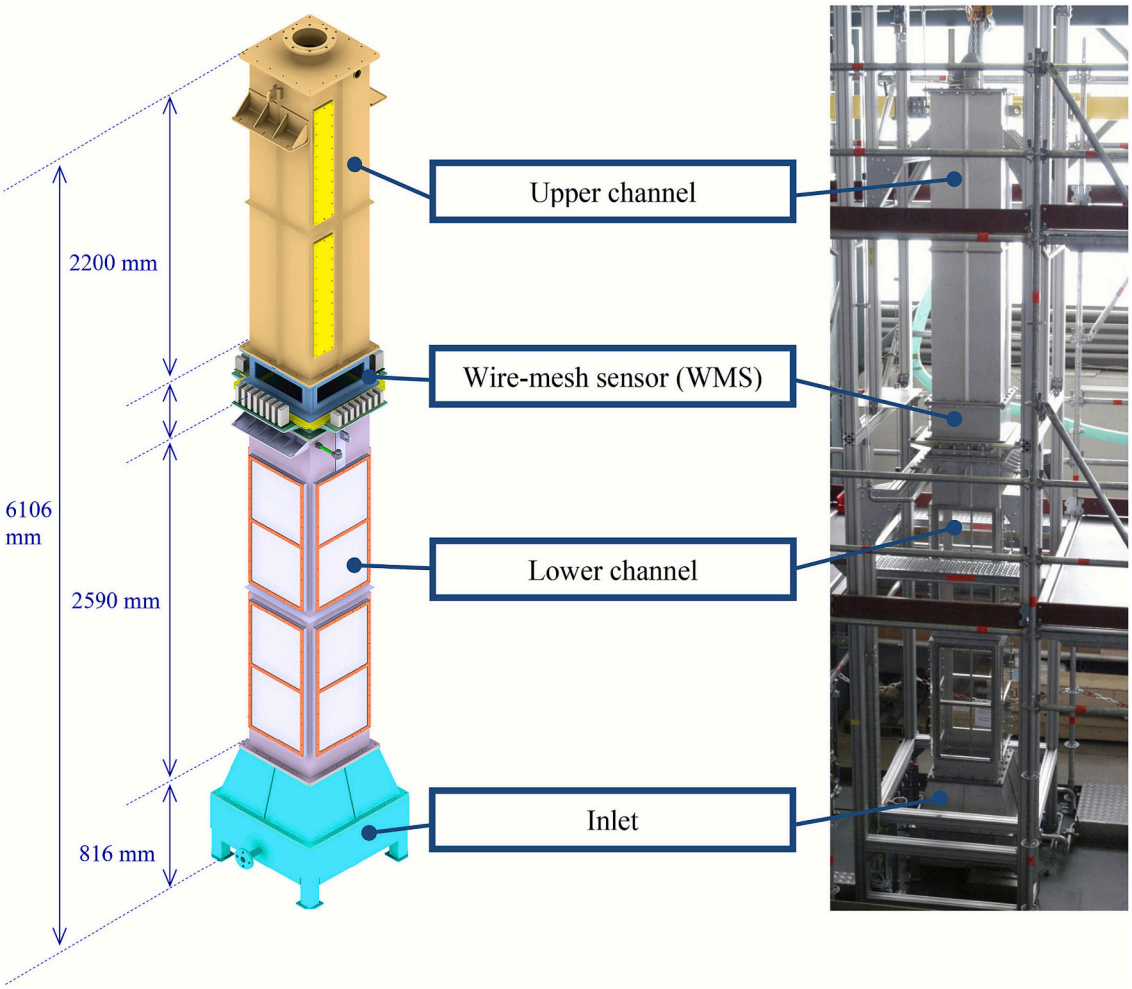


**Fig. 2.** Overview of the TRISTAN facility (Betschart, 2015).

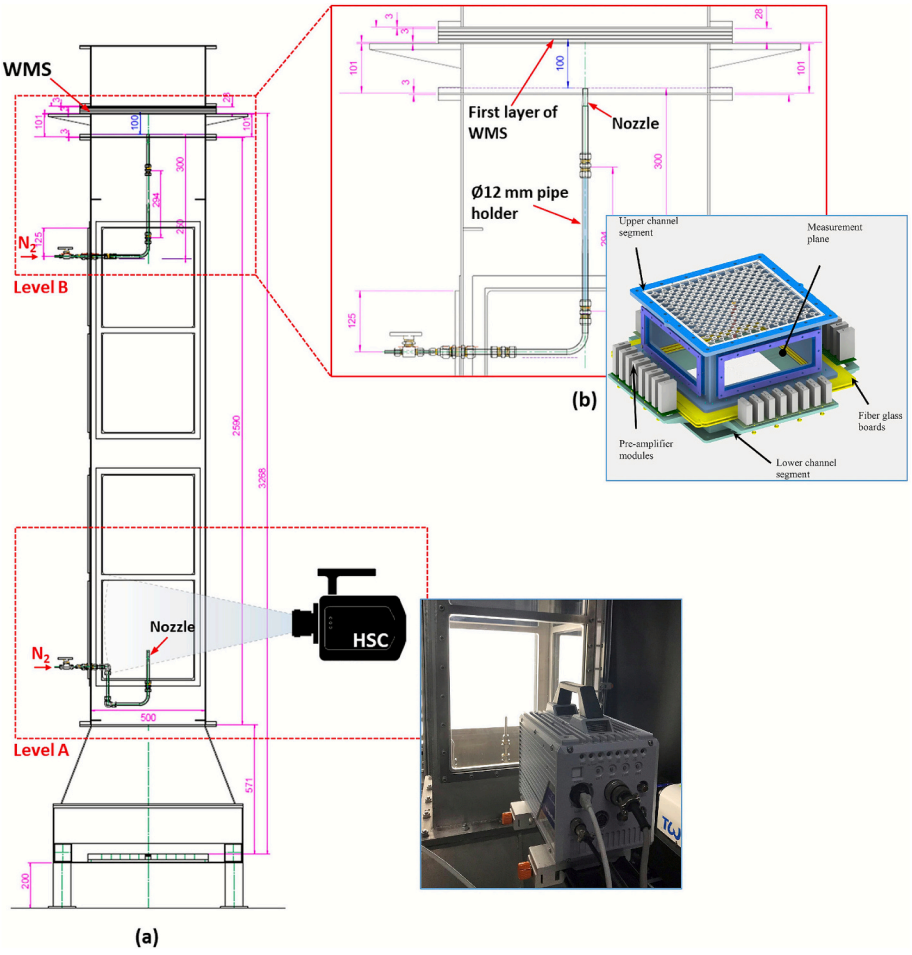


**Fig. 3.** HSC and WMS arrangement in TRISTAN facility.

requirements. On the opposite side, an LED panel is placed to provide diffuse and uniform light (Fig. 3(a)). Due to the difference in the refractive index, the light rays deflect at the gas-liquid interface. Consequently, the shadow effect is generated in the recorded images. With 1000 Hz image frequency and time recording of 5 s, all the visible dynamics and, more precisely, the globules detachment are well captured.

*2.1.1.2. Wire mesh sensor.* WMS generates cross-sectional images of phase distribution by measuring the electrical properties at each crossing point between two planes of thin conductive wires (Ghendour et al., 2020). This technique is widely used for void fraction measurement in gas-liquid two-phase flows. As shown in Fig. 4, the transmitter wires are sequentially excited by a high-frequency AC pulse, and the current received depends on the local conductivity, which reflects the gas-liquid distribution in the test section.

At the TRISTAN facility, two WMS units are installed 15 mm apart. Each sensor has two layers of 128 stainless steel wires (100 μm diameter) with 3.4 mm lateral and 2 mm axial spacing. While the full 128 × 128 configuration requires all channels of the Teletronic WMS200 system, experiments showed that a 64 × 64 configuration using the central wires is sufficient to capture all relevant bubbles. This setup enables both sensors to operate with a single WMS200 box at 1250 Hz, reducing data size and processing time. Each measurement lasted 60 s.

*2.1.2. Data processing*

Utilizing both the HSC and WMS, a substantial database encompassing both the vertical and horizontal planes of the test section can be compiled. This database yields essential parameters, including the properties of the bubbles and the Gas Void Fraction (GVF), $\alpha$. The latter is a critical parameter derived from the density function $P$, which is defined in the case of gas-liquid two-phase flow as follows (Bertola, 2003):

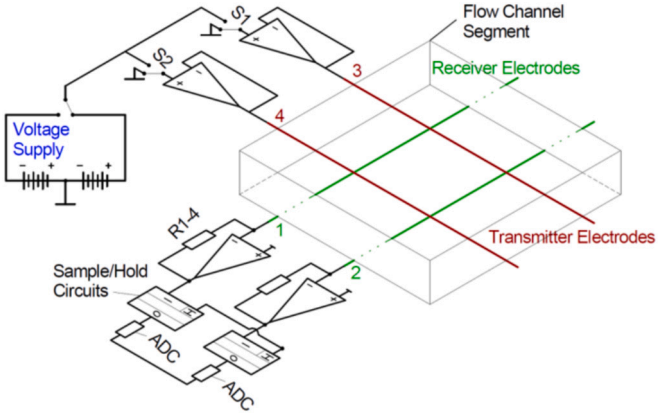


**Fig. 4.** Electrical schema of WMS working principle (Betschart, 2015).

$$P(x,y,z,t) = \begin{cases} 1 & \text{if } P(x,y,z) \in Gas \\ 0 & \text{if } P(x,y,z) \in Liquid \end{cases} \quad (1)$$

For HSC data, the density function, $P$, would be applied to the pixels of the binary images, whereas for WMS data, it corresponds to the values

at each crossing point of the sensor for every frame. Accordingly, various definitions of the GVF can be formulated by averaging the density function over spatial and/or temporal domains (Ghendour et al., 2020).

*2.1.2.1. HSC images analysis.* Different image processing steps were performed using DaVis 10 Software (LaVision GmbH) to analyze the recorded data, as shown in Fig. 5. First, the background was removed by subtracting a reference image taken without gas flow, and a Gaussian filter was applied to reduce residual noise (Process 1). The images were then cropped to the region of interest and converted to binary format using a threshold, typically between 80 and 90 %, to identify the gas–liquid interface (Process 2). Next, a segmentation tool was applied to distinguish gas and liquid phases by setting a minimum element size, producing binary images where white represents liquid and black represents gas (Process 3). At this point, the instantaneous or time-averaged GVF along lines or over the full 2D field is calculated. Finally, bubble characteristics were extracted using the ParticleMaster Shadowgraphy module, which processes multi-frame buffer files to determine the size, equivalent diameter, and velocity of individual bubbles, along with statistical measures such as average diameter and velocity (Process 4).

*2.1.2.2. WMS data analysis.* The WMS Framework Analysis Package developed by Helmholtz-Zentrum Dresden-Rossendorf (HZDR) was utilized for post-processing and analyzing the WMS data. With an intuitive graphical user interface environment, this package offers a range of integrated modules dedicated to WMS data processing, encompassing functions such as void analysis, velocity assessment, bubble identification, and bubble distribution analysis.

To derive the GVF data from the raw WMS data, the conductance of each WMS node, $u_{i,j,k}$, is normalized with respect to the conductance of the liquid, $u^{w}_{i,j,k}$ (reference value). Accordingly, the relative conductance, $g_{i,j,k}$, is described as follows:

$$g_{i,j,k} = \frac{u_{i,j,k}}{u^{w}_{i,j,k}} \tag{2}$$

Subsequently, Maxwell's law is employed (Maxwell, 1881), linking the GVF, $\alpha_{i,j,k}$, to the normalized conductance $g_{i,j,k}$ for each node in the sensor plane, as expressed in eq. (3).

$$\alpha_{i,j,k} = \frac{1 - g_{i,j,k}}{1 + \frac{1}{2}g_{i,j,k}} \tag{3}$$

The conversion from normalized conductance to GVF in Eq. (3) follows a Maxwell-type effective-medium approach at the WMS cell scale. Each sensor node is treated as a locally homogenized two-phase mixture with a single effective conductivity, where the liquid is the continuous conducting phase and the gas is effectively non-conducting. A uniform liquid conductivity is assumed during the measurement.

During the processing, the histogram calibration was applied to compute the reference value of liquid conductance, $u^{w}_{i,j,k}$, to avoid the effect of conductivity change during the experiment due to the change in temperature. Work conducted in (Prasser and Häfeli, 2018) proved that the calculation of the GVF using Eq. (3) without eliminating the negative values due to overshoots of the conductance yields higher accuracy. Accordingly, this approach, which is called "Maxwell not cut", was applied for void calculation. Utilizing the raw data from the second sensor, additional valuable information can be extracted such as the averaged velocity of the gas phase. This is accomplished by cross-correlating the signals from the two sensors.

To assess the consistency of the WMS measurements, the injected gas flow rate was reconstructed from the WMS data by integrating the product GVF × Velocity. This evaluation was performed for both nozzle diameters and for all WMS positions considered. The reconstructed flow rates were found to be in reasonable agreement with the flow rate set by the mass flow controller, with deviations within approximately 23 % over the investigated operating range.

### 2.2. SAAB facility – Aerosol retention experiments

The aerosol retention experiments were conducted at the SAAB facility at Forschungszentrum Jülich (FZJ). SAAB is a large-scale stainless steel test facility with an inner diameter of 1.5 m and a total height of up to 8 m, operating at ambient pressure (Fig. 6). It is specifically designed for high-quality, well-controlled aerosol experiments, allowing the generation of various aerosol types and particle sizes.

The SAAB facility and its aerosol generators were originally designed for high-flow and high-concentration experiments, which differ significantly from the low-flow conditions of our intended experiments. Accordingly, modifications were made to the injection and outlet sampling systems.

In these experiments, the water submergence level is 30 cm, so only the bottom and first ring segment of the facility were used, as shown in Fig. 6, allowing better control and flexibility. Due to the low injection flow rate and the large free volume above the water, there was a risk of gas deceleration and particle settling back at the surface. To prevent this, a Casing Tube (CT) was installed, enclosing the nozzle inside the water. The CT is made of stainless steel and has an inner diameter of 32 cm and a length of 180 cm. It ensures that the injected gas flows within the tube rather than the full SAAB cross-section (Fig. 6).

Despite reducing the volume above the water, low momentum inside the CT still led to particle settling. Additionally, the membrane filter at

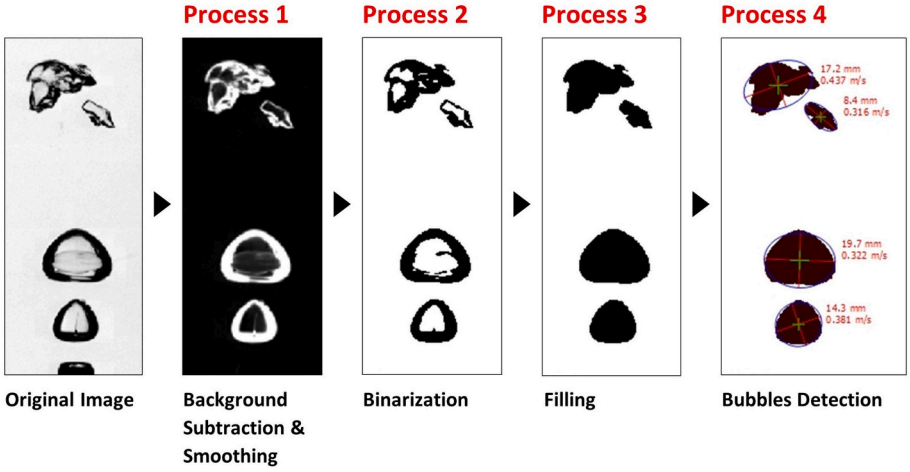


**Fig. 5.** Image processing procedures followed in DaVis 10.

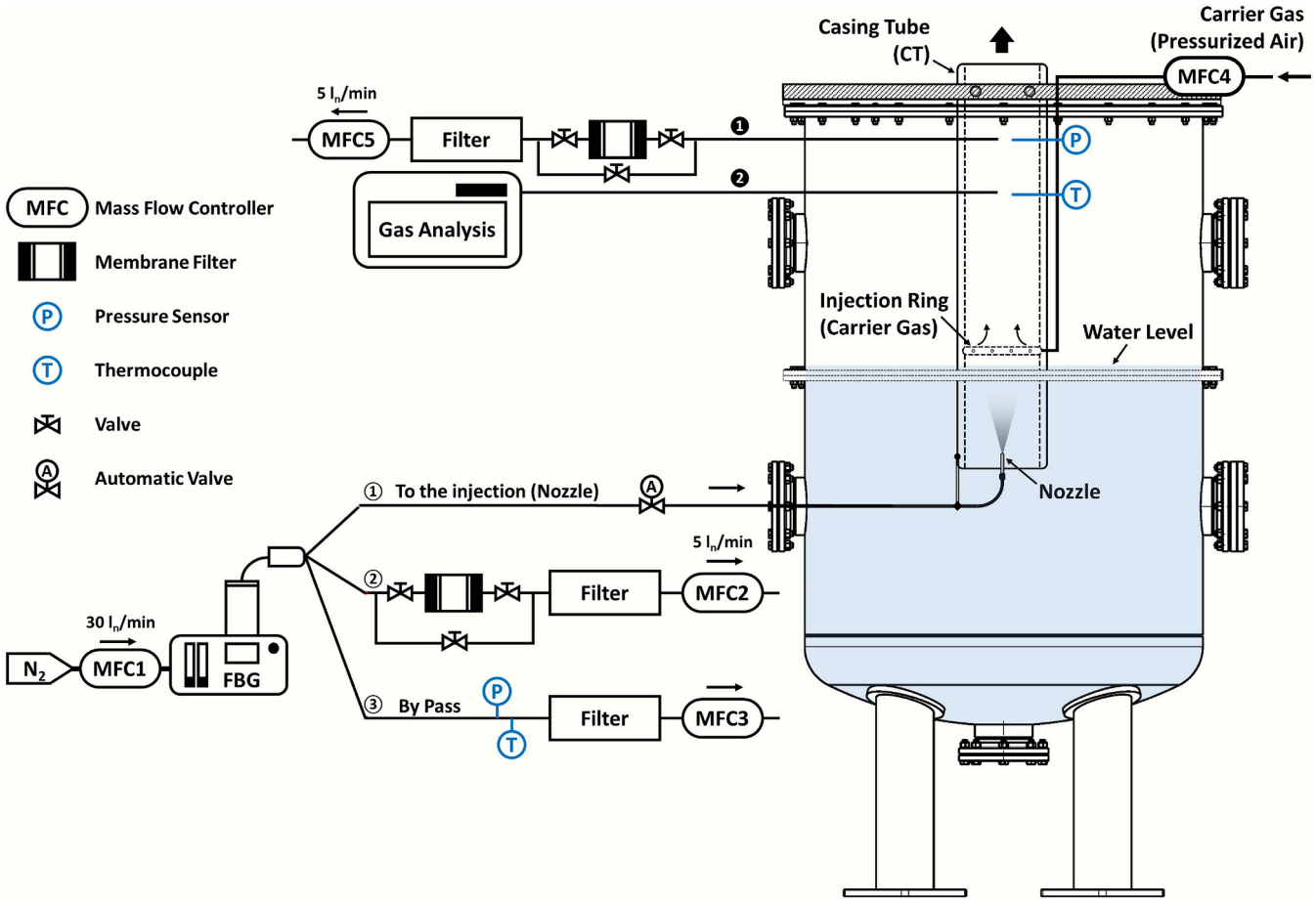


**Fig. 6.** Design of SAAB facility for aerosol retention experiments.

the outlet required a flow rate of 5 $l_n$/min for sampling. To meet this need, a Carrier Gas (CG) system was added inside the CT. Pressurized air, controlled by a mass flow controller (MFC4), was injected through a ring with eight 1 mm holes angled at 45° and located 10 cm above the water surface to minimize water droplet entrainment.

The aerosol injection and sampling system was designed to ensure stable operation under low flow rate conditions. Nitrogen is supplied at 30 $l_n$/min to the aerosol generator, and the flow is divided into three lines: (1) for vessel injection, (2) for membrane filter measurement, (3) bypass line to control the flow in the injection line. The outlet sampling system follows a similar layout, with dedicated lines for membrane filter sampling, flow control, and gas analysis.

### 2.2.1. Silicon dioxide ($SiO_2$) particles

In all experiments, mono-disperse Silicon Dioxide (Silica, $SiO_2$) spherical particles are used. The particles are manufactured by the company Nippon Shokubai in Japan (www.shokubai.co.jp). The aerosol particles have a very narrow particle size distribution with a specific gravity is 2.0. Table 1 shows the actual particle characteristics including the Aerodynamic Mass Median Diameter (AMMD) based on the certificate of analysis of the powder delivered.

**Table 1**
Actual data of $SiO_2$ based on analysis.

| Product | Average Diameter [μm] | | AMMD [μm] |
|---|---|---|---|
| | Specification | Analyzed | |
| KE-P50 | 0.50–0.60 | 0.54 | 0.76 |
| KE-P100 | 0.90–1.30 | 1.02 | 1.44 |
| KE-P250 | 2.25–2.75 | 2.56 | 3.62 |

### 2.2.2. Measurement

The membrane filter is used to measure the mass concentration of $SiO_2$ in the gas flow. For this purpose, a borosilicate glass microfiber filter (Pallflex) with suitable pore size was selected to retain the target particles. During each test, gas is sampled for 20 min and passed through the filter, which captures the $SiO_2$ particles. After sampling, the filter is weighed using a precision balance. The mass concentration is then calculated by dividing the collected $SiO_2$ mass by the total volume of gas that passed through the filter.

## 2.3. Experimental design and test conditions

To ensure identical flow geometry and initial injection conditions, both experimental campaigns conducted in the TRISTAN and SAAB facilities employed the same injection nozzles, with inner diameters of 5 mm and 10 mm. In addition, identical initial conditions were maintained in both facilities, with experiments performed at ambient pressure and temperature (1 bar, ≈ 25 °C).

In the TRISTAN facility, a parametric study was carried out to characterize the hydrodynamics of the globule regime. For each nozzle, nitrogen flow rates between 1 and 10 $l_n$/min were investigated. In this work, the gas flow rate is reported in normal liters per minute ($l_n$/min), which is the control and output unit of the mass flow controller and represents a volumetric flow rate normalized to standard reference conditions (0 °C and 1 atm).

In contrast, the aerosol retention experiments performed in the SAAB facility were limited to a reduced set of nitrogen flow rates (1, 5, and 10 $l_n$/min) for each nozzle and for each particle size (0.5, 1, and 2.5 μm). This reduced test matrix reflects the significantly higher experimental complexity associated with aerosol generation and sampling in a large-

scale facility, including extended cleaning procedures and water replacement when changing particle size. These experiments represent a new capability for the SAAB facility, as dedicated low-flow-rate injection and aerosol sampling systems had to be developed and implemented to operate under globule regime conditions, which were outside the original design scope of the facility.

## 3. Experimental hydrodynamics results

This section summarizes the main findings from the hydrodynamics experiments in TRISTAN facility, focusing on the flow behavior and the globule formation under different injection conditions.

### 3.1. Flow regime

#### 3.1.1. HSC experiments

*3.1.1.1. Qualitative aspects.* For the full range of gas flow rates investigated, the flow remained in an aperiodic globule regime. This regime is characterized by unsteady and irregular gas-structure dynamics driven by globule–globule interactions, including coalescence, deformation, and breakup. Fig. 7 and Fig. 8 are sequential images with a time step of 50 ms for the flow regimes recorded with 10 and 5 mm nozzles at gas flow rates equal to 1, 5, and 10 $l_n$/min, respectively.

At the flow rate of 1 $l_n$/min, the images of 10 mm nozzle (Fig. 7) show the interaction and aggregation of two globules in the region close to the nozzle. However, the collision force is not sufficient for the globules to coalescence. At the same time, we can see the creation of small bubbles due to the vibration of the globules surface. After a few milliseconds, the aggregated globules segregate and break up into smaller bubbles. Increasing the flow rate to 5 $l_n$/min initiates the globules coalescence, forming a larger bubble which is characterized by chaotic motion and unstable surface vibration. This leads to globule breakup and the creation of small bubbles. Furthermore, the wake effect at this flow rate starts to play a serious role in the globules formation and bubbles behavior.

At the injection region and after detachment of the first globule (leading globule), the wake region enhances and accelerates the creation of the next globule (trailing globule) in an elongated shape. This leads to the interaction and coalescence of the trailing globule with the leading globule even before the detachment. This phenomenon becomes stronger at a flow rate of 10 $l_n$/min, where the coalescence of three or even four globules can take place in the injection region. This big globule rises and breaks up, creating a swarm of small bubbles.

Regarding the 5 mm nozzle experiments (Fig. 8), the images revealed a high frequency of globule formation. This led to the aggregation of more than two globules at a flow rate of 1 $l_n$/min. However, the collision force was not strong enough for globule coalescence. The rapid formation of globules at higher flow rates caused them to be close, amplifying the wake effect and consequently elongating the globules.

*3.1.1.2. Quantitative results.* The post-processing of the high-speed images provides essential insight into the flow characteristics under each operating condition. Fig. 9 presents the time-averaged two-dimensional GVF fields measured in the camera plane for both nozzle diameters and selected flow rates, with the z-axis representing the distance from the nozzle tip. Each field represents the local gas void fraction at every pixel of the measurement plane, obtained by time-averaging the binary gas–liquid phase images (Fig. 5, Process 3) over the full acquisition period.

In all cases, the GVF distribution exhibits a jet-like structure characterized by a high-GVF core originating at the nozzle exit. This high GVF region corresponds to the successive formation of globules at the nozzle tip, where the gas phase remains highly concentrated. With increasing distance from the nozzle, the peak GVF gradually decreases while the distribution spreads laterally. This evolution is associated with globule deformation and breakup. As the globules rise, they fragment into smaller bubbles, which enhances lateral dispersion and leads to a progressive reduction of the local void fraction along the nozzle centerline.

An increase in the gas flow rate leads to higher GVF values near the nozzle and to a larger spatial extent of the gas-dominated region. This behavior is attributed to the increased injection momentum, which promotes more frequent formation of larger globules and delays their breakup, thereby maintaining a dense gas core over a longer axial distance. As a result, both the penetration height and the lateral spread of the GVF increase with increasing flow rate.

The effect of nozzle diameter is most pronounced in the nozzle injection region. For the same gas flow rate, the 10 mm nozzle generates a wider GVF distribution close to the injection point, as it produces larger globules compared to the 5 mm nozzle. In contrast, the 5 mm nozzle results in a higher exit velocity and thus higher local momentum, leading to the formation of smaller globules with higher detachment frequency. This increases globule–globule interactions along the nozzle centerline and enhances wake effects, resulting in a more elongated gas-dominated region in the axial direction. Further downstream, the GVF distributions for both nozzles become increasingly similar, indicating that the flow evolution is governed primarily by buoyancy and

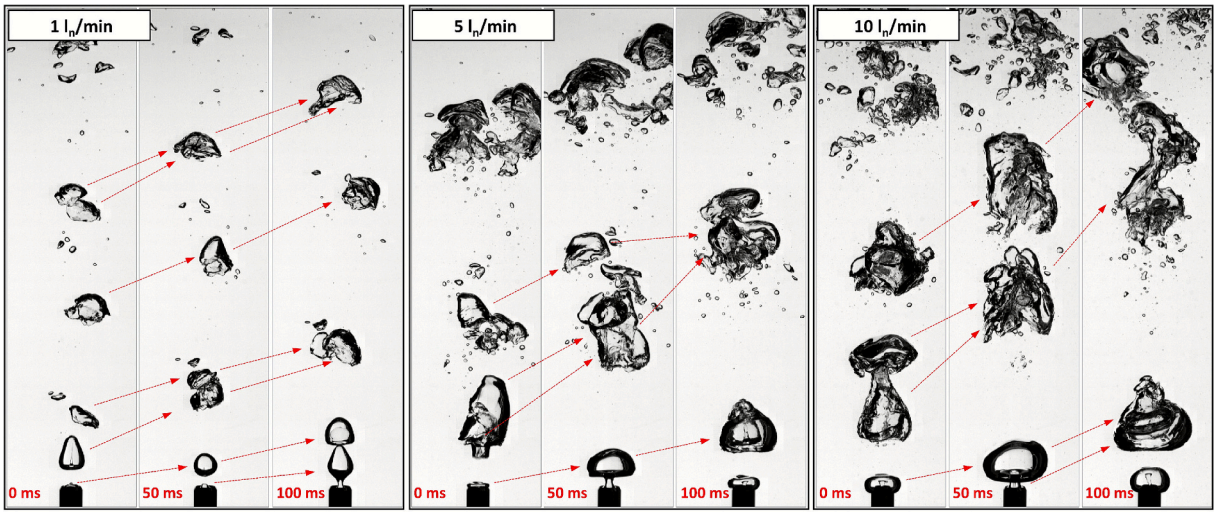


**Fig. 7.** Flow regime for 10 mm nozzle diameter at gas flow rates of 1, 5, and 10 $l_n$/min.

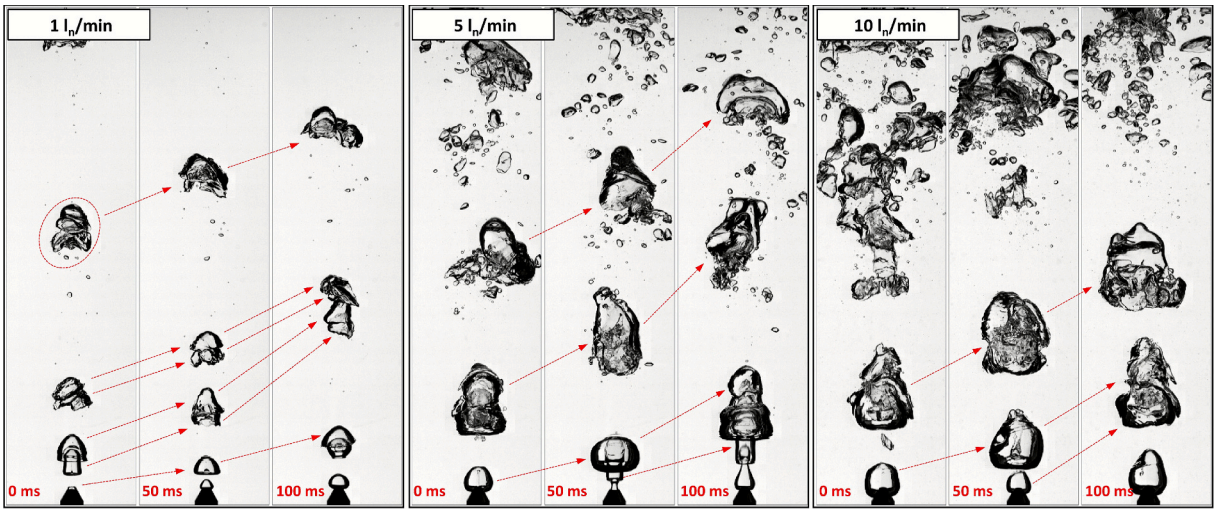


**Fig. 8.** Flow regime for 5 mm nozzle diameter at gas flow rates of 1, 5, and $l_n$/min).

interfacial interactions rather than the chosen nozzle diameter.

### 3.1.2. *WMS experiments*

The time-averaged two-dimensional GVF fields derived from the HSC images (Fig. 9) provide a useful visualization of the global flow development. However, the HSC-based GVF is obtained in the camera plane (x–z) and represents a projected view of the gas phase, i.e., the contributions of globules and bubbles distributed over the depth of the measurement volume are mapped onto a single plane. As a result, the HSC-based GVF is primarily qualitative/semi-quantitative and may overestimate local void fraction levels in regions where multiple gas structures overlap along the line of sight. For a more quantitative characterization, the void fraction distribution is therefore evaluated using the wire-mesh sensor (WMS), which provides local measurements of GVF over a cross-section perpendicular to the main flow direction (x–y plane). The WMS thus provides spatially resolved, cross-sectional GVF data which are more suitable for quantitative analysis and CFD validation.

All the WMS data were processed for each case. For instance, Fig. 10 presents 3D phase distribution for 10 mm nozzle and a flow rate of 10 $l_n$/min. Fig. 10(a) is a 3D reconstruction of space-time images at z = 40, 100, and 200 mm where the vertical axis represents the time. At z = 40 mm, globule coalescence is visible in the image. However, distinguishing individual globules is challenging due to the low resolution of WMS compared to HSC. The HSC recording revealed that globule coalescence initiates before z = 40 mm. Consequently, extracting the globule detachment frequency from the WMS data is unattainable. As expected, the space-time image at z = 100 and 200 mm showed the breakup of the globules and the creation of small bubbles.

Fig. 10(b) shows the corresponding cross-sectional time-averaged GVF distributions at z = 40, 100, and 200 mm. The quantitative GVF fields obtained from the WMS are, on average, approximately axisymmetric about the nozzle centerline, indicating that the mean phase distribution is radially uniform around the injection axis. The GVF also follows the same qualitative trend as the HSC-based GVF fields (Fig. 9). At z = 40 mm, the GVF displays a sharp central peak with a maximum value of about 36 %. With increasing axial distance, the peak broadens and its magnitude decreases, reaching approximately 15 % at z = 200 mm, consistent with enhanced lateral dispersion and breakup of the gas structures.

The effect of the nozzle diameter and the flow rate on the GVF distribution are analyzed and presented in Fig. 11. This figure illustrates the time-avereged GVF along the horizontal line at z = 40, 100, and 200 mm for flow rates of 1, 5, and 10 $l_n$/min. In all cases, the GVF decreases monotonically from a maximum at the centerline (x = 0) to zero at the edge of the gas-affected region. Increasing the flow rate results in higher peak GVF values and a larger radial extent of the gas-affected region at all axial positions.

Regarding the nozzle diameter effect, the differences are most pronounced in the near-field region (z = 40 mm). For the same flow rate, the 5 mm nozzle exhibits a higher centerline GVF, whereas the 10 mm nozzle produces a broader distribution with a larger affected radius. This nozzle effect progressively diminishes with increasing distance from the nozzle. For example, at z = 200 mm, the GVF profiles for the 10 mm nozzle become comparable to those obtained with the 5 mm nozzle, indicating that the far-field void fraction distribution is less sensitive to the nozzle diameter.

Fig. 12 provides an overview of the time-averaged velocity of the gas phase along a horizontal line at z = 40, 100, and 200 mm for gas flow rates of 1, 5, and 10 $l_n$/min. Overall, velocity increases with the flow rate and decreases as we move away from the nozzle. Along the x-axis, the velocity gradually drops for the same flow rate. This is attributed to globule coalescence, where buoyancy enhances the rise velocity of the globules. At higher levels, smaller globules flow at lower velocities. Notably, there is a minor effect of nozzle diameter observed on the velocity profile, with a slight increase in velocity for the case of 5 mm nozzle.

Fig. 12 summarizes the time-averaged gas-phase axial velocity derived from the WMS along a horizontal line at z = 40, 100, and 200 mm for gas flow rates of 1, 5, and 10 $l_n$/min. It should be noted that this WMS “gas velocity” represents the velocity of the gas phase inferred from the WMS signals and therefore does not necessarily correspond to the rise velocity of bubbles/globules. Overall, the measured gas-phase velocity increases with increasing flow rate and decreases with radial distance from the centerline. With increasing distance from nozzle tip, the profiles become broader and the peak values reduce, reflecting the progressive breakup and dispersion of the gas structures to smaller bubbles with low velocity.

At z = 40 mm, the velocity profiles for 5 and 10 $l_n$/min exhibit a pronounced centerline peak. This feature is attributed to wake-induced interactions, which promote globule elongation and accelerate trailing globules along the centerline. The HSC images indicate that this elongation becomes significant once globule coalescence initiates at the nozzle exit, which is first clearly observed from 5 $l_n$/min onward. Overall, the nozzle-diameter effect on the velocity profiles is minor. However, the 5 mm nozzle yields slightly higher velocities, consistent with its higher exit velocity at the same flow rate.

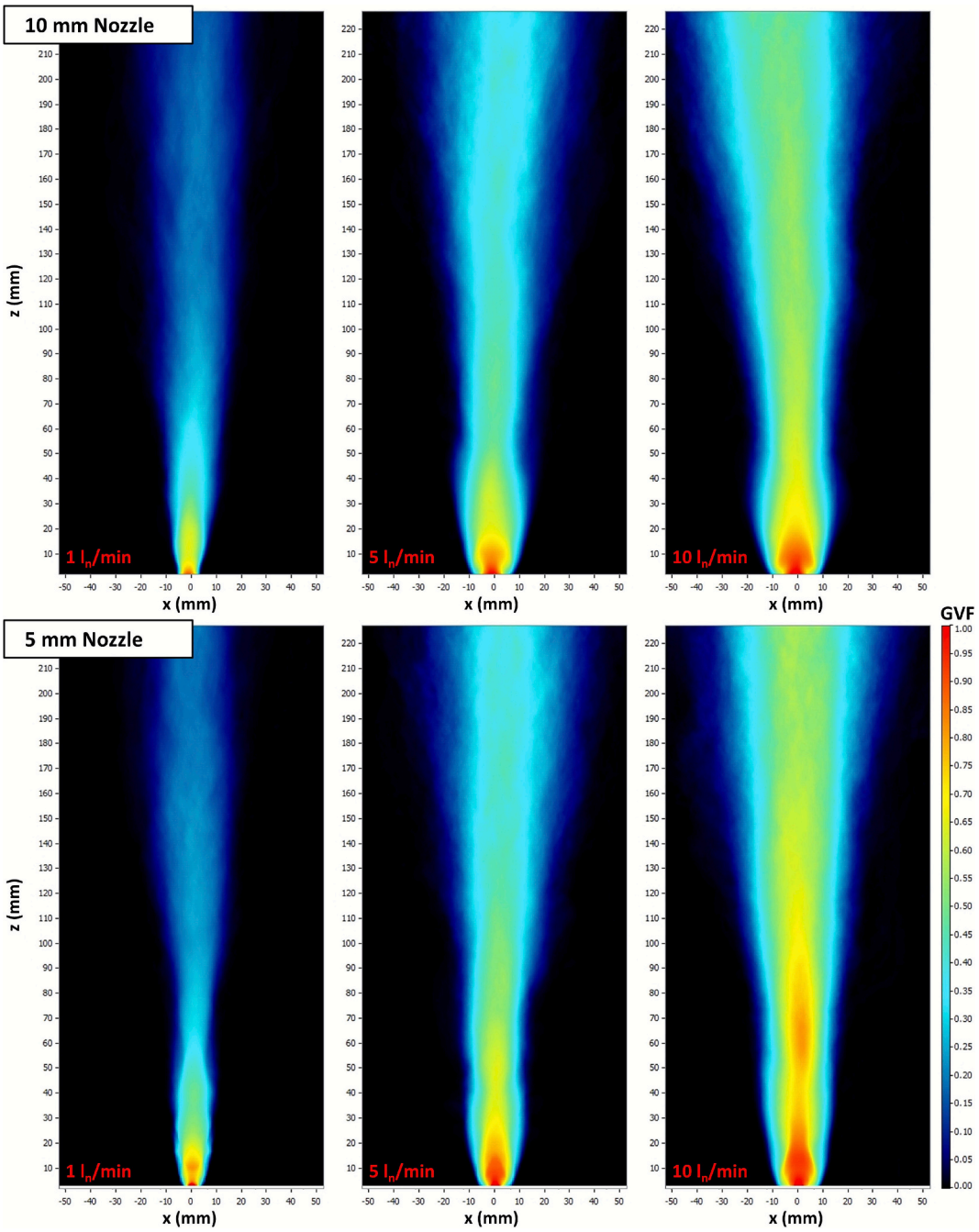


**Fig. 9.** Time-averaged two-dimensional GVF field from the HSC images for the tests with 10 and 5 mm nozzles and at gas flow rates of 1, 5, and 10 $l_n$/min.

### *3.2. Phenomena in the injection region*

The chaotic behavior of this regime (bubble aggregation, coalescence, and breakup) makes it difficult to track individual bubbles and extract their properties using HSC and WMS data. To simplify the analysis, the focus was placed on the formation of the first globule at the moment of detachment in the injection region, where the globule typically has a quasi-axisymmetric shape. This allows for a more accurate estimation of its diameter and volume, although coalescence still presents challenges even in this simplified scenario.

A dedicated analysis approach was developed, including clear definitions of key terms. Detachment is defined as the moment when the neck between the globule and the nozzle breaks, marking the initiation of a new globule. At this point, properties such as diameter, volume, shape, and velocity are determined. The detachment frequency refers to the number of such events per second. However, since multiple globules may form between two detachments, the globule frequency is introduced to represent the actual number of globules formed per second. Only HSC data were used, as the WMS does not resolve the region close to the nozzle accurately enough for this analysis.

Fig. 13 presents the image processing method developed for this purpose. A custom algorithm removes background bubbles and isolates the first globule after each detachment. Two indicators were used to identify and track these events. The first, ind1 (Fig. 13(a) and (b)), calculates the gas-phase pixel average along a horizontal line, detecting globule creation, as shown in Fig. 13(c). The second, ind2 (Fig. 13(a) and (b)), monitors a fixed point near the nozzle; detachment is identified when ind2 drops from 1 to 0, as represented in Fig. 13(d). The final output, (Fig. 13(e)), shows the globule formation timeline and detachment events, allowing for the calculation of globule and detachment

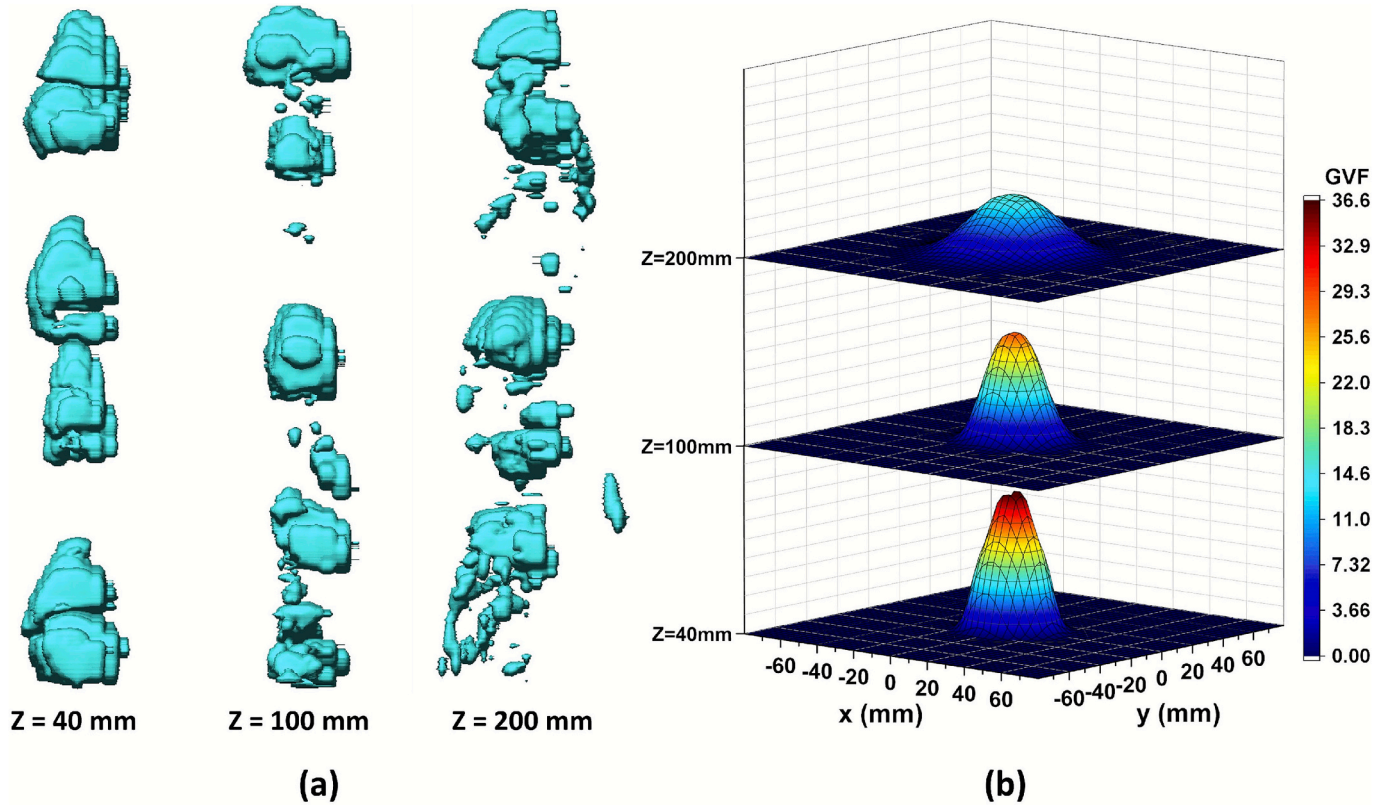


**Fig. 10.** 3D gas phase distribution for 10 mm nozzle diameter and flow rate of 10 $l_n$/min, at z = 40, 100, and 200 mm; (a) 3D reconstructed space-time images, (b) cross-sectional time averaged GVF.

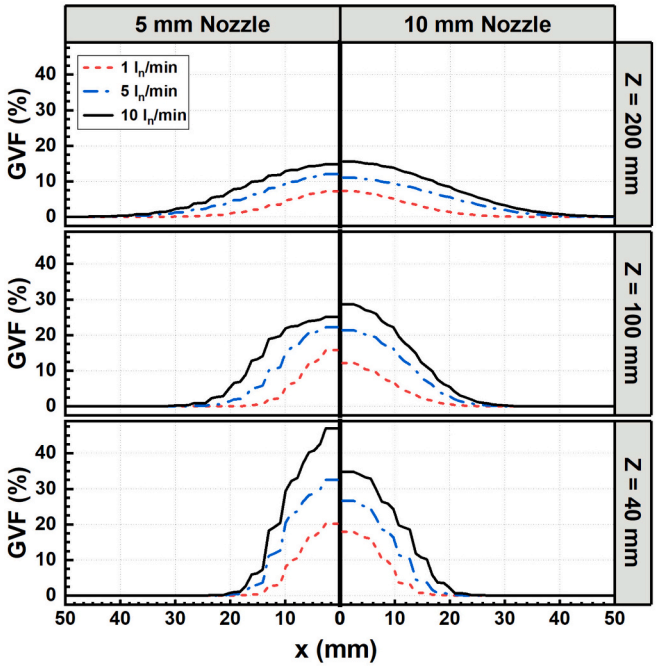


**Fig. 11.** Time-averaged GVF distribution along the horizontal line for 10 mm nozzle (right graphs) and 5 mm nozzle (left graphs), at z = 40, 100, and 200 mm, and gas flow rates of 1, 5, and 10 $l_n$/min.

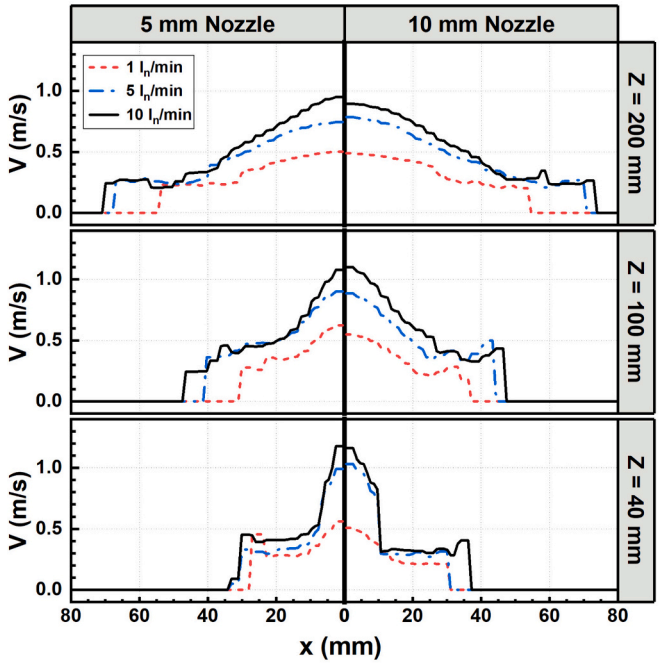


**Fig. 12.** Time-averaged velocity along the horizontal line for 10 mm nozzle (right graphs) and 5 mm nozzle (left graphs), at z = 40, 100, and 200 mm, and gas flow rates of 1, 5, and 10 $l_n$/min.

frequencies. This method also enables estimation of how many globules are generated between detachments and the associated probability distribution.

To provide a general characterization, we present the properties of the globule at the detachment event as a function of the dimensionless Weber number, *We*, which is the ratio of the inertial force to the surface tension force. It is defined as:

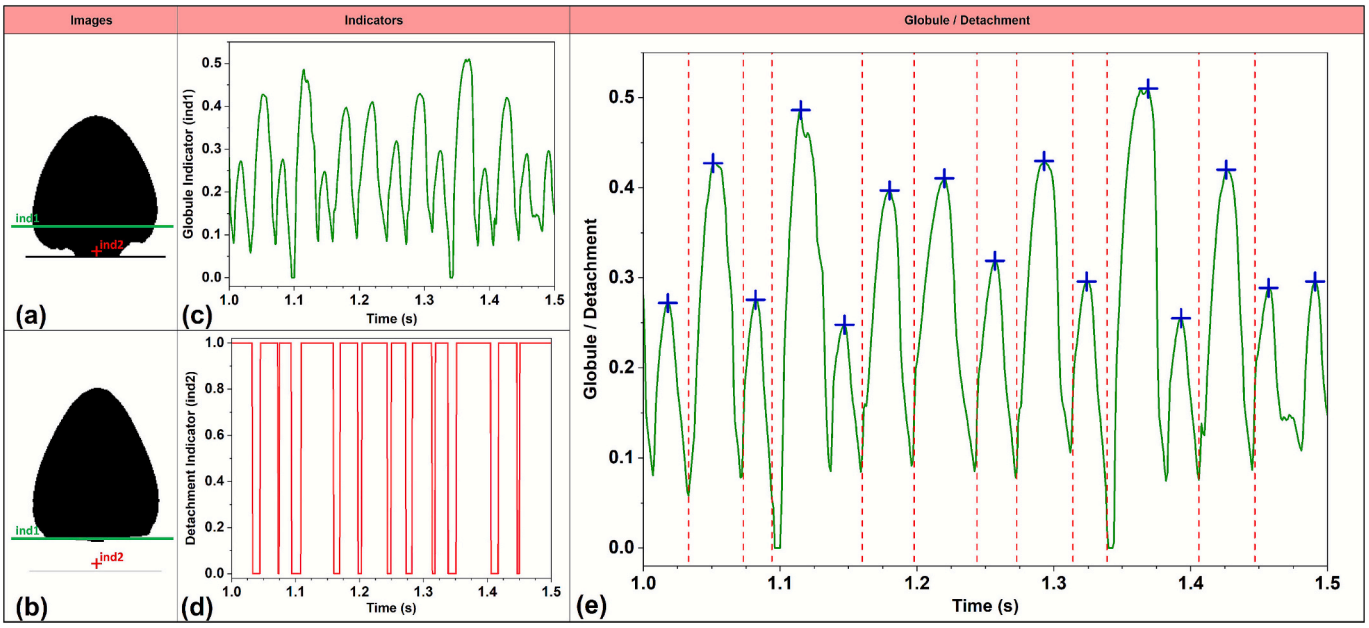


**Fig. 13.** Developed globule tracking algorithm: (a) indicator locations (ind1 line, ind2 point) for a globule prior to detachment, (b) indicator locations at the detachment instant, (c) ind1 time series (globule formation), (d) ind2 time series (detachment), and (e) combined output showing globule events (markers) and detachment instants (red dashed lines) used to compute formation and detachment frequencies. (For interpretation of the references to colour in this figure legend, the reader is referred to the web version of this article.)

$$We = \frac{\rho V^2 D}{\sigma} \tag{4}$$

Above $\rho$ is the density of the gas, $V$ is velocity, $D$ represents ther characteristic length which is here the nozzle diameter and $\sigma$ is the surface tension of the liquid.

Fig. 14 summarizes the globule behavior at detachment in relation to the Weber number, including globule diameter $D_b$, velocity $V_b$, and the frequency of formation $f_b$ and detachment $f_{det}$.

For a flow rate between 1 and 10 $l_n$/min, the Weber number reaches approximately 1 for the 10 mm nozzle and up to 7.3 for the 5 mm nozzle. Overall, both globule diameter and velocity increase with the Weber number in a nonlinear fashion. This increase is steep within the low

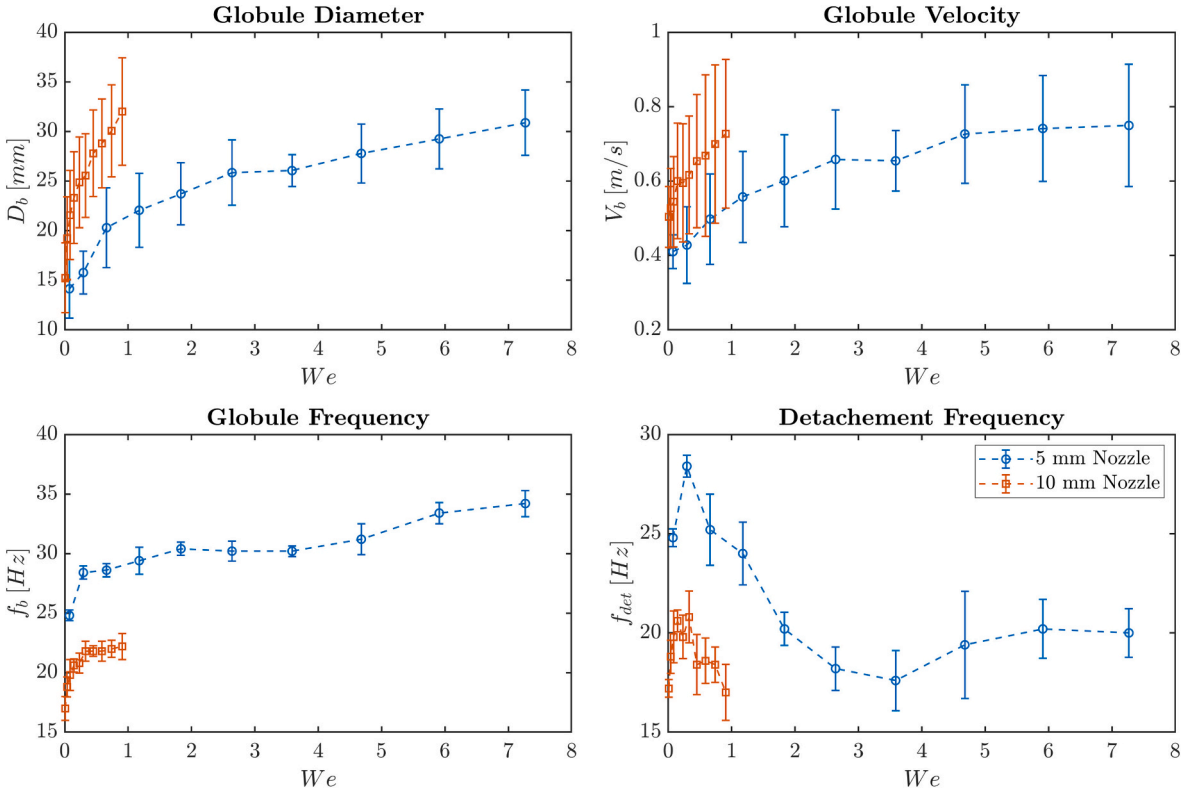


**Fig. 14.** Globule characteristics at detachment as a function of *We* number.

Weber number range (0–1), after which the growth rate becomes more gradual as *We* continues to rise.

Focusing on the Weber number range of 0 to 1 (where data is available for both nozzles), the 10 mm nozzle consistently exhibits larger globule diameters and higher velocities compared to the 5 mm nozzle. For example, at $We = 1$, the 10 mm nozzle produces globules with a diameter of approximately 33 mm and a velocity of 0.7 m/s, while the 5 mm nozzle results in a globule diameter of about 23 mm and a velocity of 0.55 m/s.

Regarding the globule formation frequency, the 10 mm nozzle shows an increase up to approximately 22 Hz as the Weber number reaches $We = 0.3$, after which the frequency stabilizes. A similar trend is observed for the 5 mm nozzle: the frequency increases from 25 Hz to about 28.5 Hz within the Weber number range of $We = 0$ to $We = 0.3$, then remains relatively constant between $We = 0.3$ and $We = 4$. Beyond this range, the frequency gradually increases again, reaching approximately 34 Hz at $We = 7.3$.

Overall, the 5 mm nozzle consistently exhibits higher globule formation frequencies compared to the 10 mm nozzle. This behavior aligns with the smaller globule diameters produced by the 5 mm nozzle, which allows for more frequent formation events.

For the detachment frequency, within the range of $We = 0$ to $We = 0.3$, the values match those of the globule formation frequency. This indicates that no coalescence occurred at the detachment event, and each formed globule was fully detached. However, beyond this range, the detachment frequency decreases with increasing *We*, suggesting that globule coalescence becomes more significant, preventing complete detachment of each formed globule. In the case of the 5 mm nozzle, the detachment frequency begins to increase again slightly after We = 4, which coincides with the point where the globule formation frequency also starts to rise.

From the presented results, it is evident that the Weber number alone is not sufficient to fully characterize or normalize the globule behavior at detachment, as the 5 mm and 10 mm nozzles yield significantly different values. However, it is noteworthy that all measured characteristics exhibit similar trends across both nozzle sizes. The data for the two nozzles appear to follow the same overall pattern, differing mainly by an offset or scaling factor.

Considering this observation, it was found that the results for the 5 mm and 10 mm nozzles can be related through a scaling factor corresponding to the square root of the diameter ratio.

For instance, multiplying the globule diameter and velocity obtained from the 5 mm nozzle by the factor $\sqrt{D_{10}/D_5} = 1.4142$ results in data that aligns well with the range observed for the 10 mm nozzle. Similarly, applying the inverse factor $\sqrt{D_5/D_{10}} = 0.7071$ to the diameter and velocity values from the 10 mm nozzle yields a close match with the data from the 5 mm nozzle. For the globule formation and detachment frequencies, the scaling follows an inverse relationship.

Fig. 15 illustrates this concept by presenting a scaling factor applied to each globule characteristic. Specifically, the globule diameter and velocity are scaled using the factor $\sqrt{10/D_N}$, while the globule and detachment frequencies are scaled using $\sqrt{D_N/10}$, where $D_N$ is the nozzle diameter (either 10 mm or 5 mm).

In this representation, the data are normalized relative to the 10 mm nozzle. This means the figure displays the actual measured values for the 10 mm nozzle, while the data from the 5 mm nozzle are adjusted by the corresponding scaling factor. The results in a collapse of the data around a single curve, indicating a consistent geometric relationship between the two nozzle sizes across all measured characteristics.

To further investigate this finding, we have considered also data from work of Farhat at al (Farhat et al., 2023). In this work, the authors performed similar experiment at room temperature with 2 and 5 mm nozzles for We range up to 67. We have estimated the equivelant globule diameter from the presented globule volume and we have presented them along with our data for globule diameter in Fig. 16(a). The main results show that the nozzle diamter has strong effect on the globule diamter for the same *We* number. However, we can see a good match between our data for the 5 mm nozzle with 5 mm nozzle data of Farhat et al.

In Fig. 16(b), we applied the same concept and multplied all the data to the factor of $\sqrt{10/D_N}$ meaning that all the data are presented relative to the 10 mm nozzle. It is interesting to note that the data collapse around a single parabolic curve as a function of *We*. The fit for all the data is as follows:

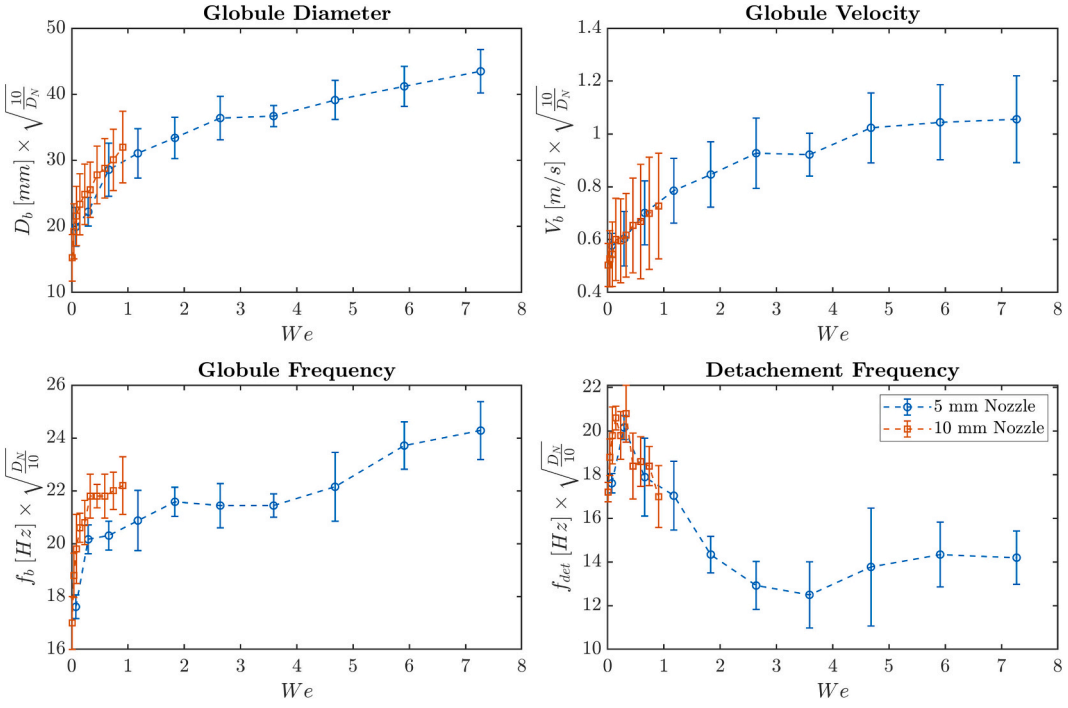


**Fig. 15.** Globule characteristics at the detachment as a function of *We* number after applying the scaling factor.

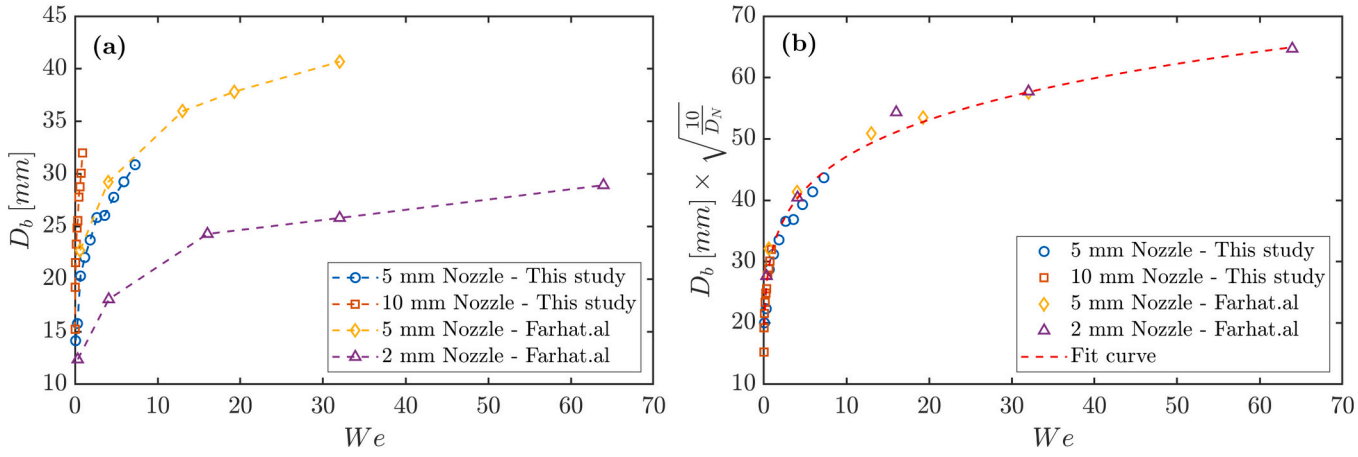


**Fig. 16.** Globule diameter at the detachment for different nozzles as a function of *We* number before (left) and after (right) applying the scaling factor.

$$D_b \times \sqrt{10/D_N} = 31.65 \times We^{0.1729} \tag{5}$$

The globule diameter as thus given by this correlation:

$$D_b = 10\sqrt{D_N}\, We^{0.1729} \tag{6}$$

Eventually, the same approach can be applied to establish correlations for other globule characteristics, such as velocity, globule frequency, and detachment frequency.

## 4. Aerosol retention experiments results

Due to the challenges related to the performance of aerosol retention experiments under low momentum injection in this large facility, tests were conducted only at 1, 5, and 10 $l_n$/min for each nozzle and particle size. For each condition, two membrane filter measurements were carried out sequentially. The retention efficiency was then calculated using:

$$\eta(\%) = 100 \times \left(1 - \frac{1}{DF}\right) \tag{7}$$

Above, DF is Decontamination Factor and represents the ratio of the aerosol inlet concentration to the outlet concentration:

$$DF = \frac{\dot{m}_{in}}{\dot{m}_{out}} \tag{8}$$

The corresponding error band was estimated based on error propagation.

Fig. 17(a) provides a summary of the aerosol retention efficiency of all the conducted tests, highlighting the effects of particle size, nozzle diameter, and flow rate. The particle removal efficiency is not very sensitive to flow rate. Indeed, a higher flow rate causes higher neck velocity when the globule is created, which should enhance particle removal. Simultaneously, the larger velocities engender larger globules with smaller surface-to-volume ratios as well as smaller residence times in the pool. These two effects cause smaller particle deposition. Hence competing effects produce similar particle removal rates, with little dependance on the flow rates used.

In addition, and as expected, larger particles exhibit a stronger tendency to be removed from the gas, with retention reaching up to 90 %

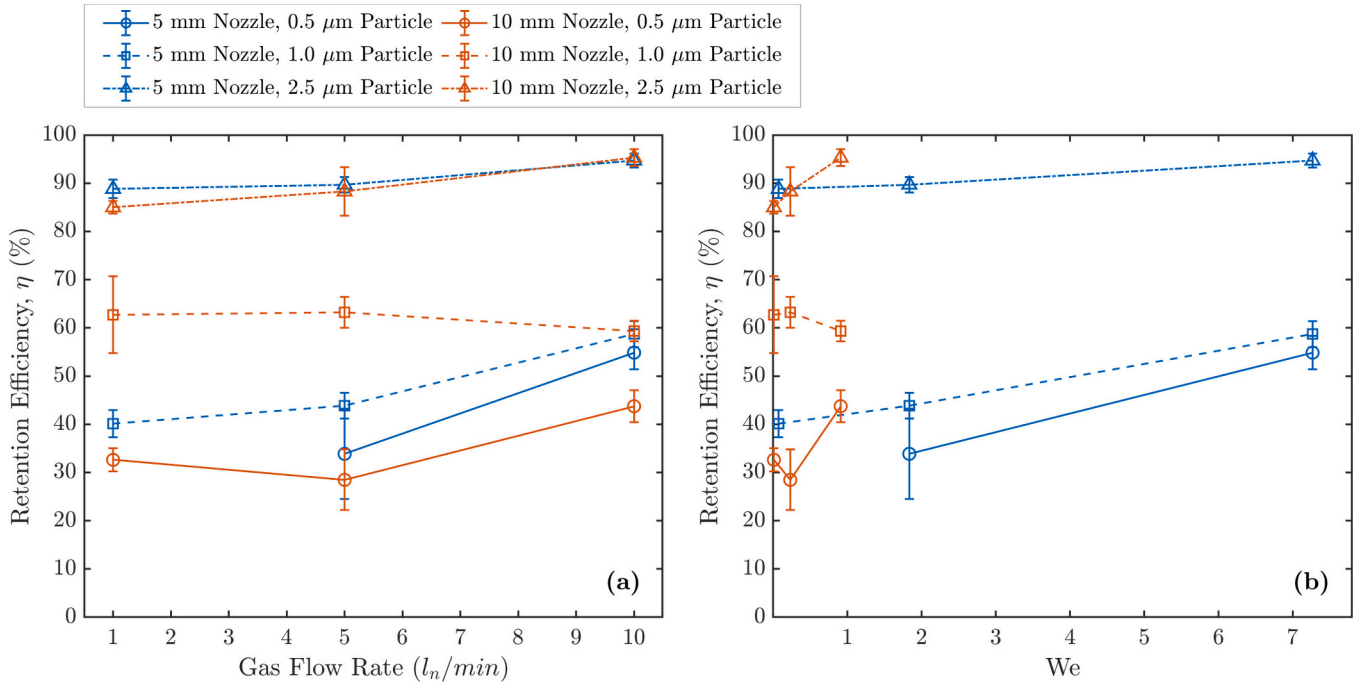


**Fig. 17.** Retention efficiency from Membrane Filter as a function of the gas flow rate (left) and *We* number (right).

for 25 μm particles. Concerning the effect of nozzle diameter, the results show mostly a slightly improved retention for the smaller nozzle. For the same flow rate, the 5 mm nozzle produces a higher globule neck velocity compared to nozzle 10 mm nozzle, hence promoting enhanced particle scrubbing. At the same time, smaller globules generated by 5 mm nozzle translate into larger residence times in the pool and an increased chance for aerosol removal. The combination of these two effects leads to larger particle retention.

However, this trend is not observed in the tests with 1 μm particles, where the 10 mm nozzle shows higher retention. This suggests that retention efficiency does not follow a clear or predictable trend with respect to nozzle size and particle size. This tendency has also been reported in the literature, where the effect of nozzle diameter and flow rate on retention shows contradictory results across different studies (Farhat et al., 2023). Further, representing the retention efficiency as function of the *We* number does not show a consistent behavior with the respect to the particle size, indicating that the Weber number alone is not sufficient to characterize aerosol retention efficiency.

From the hydrodynamics results, the difference between the two nozzles is most evident in the region near the nozzle. Ultimately, to fully understand the influence of nozzle size on retention, a deeper analysis of globule formation and detachment dynamics in relation to the underlying retention mechanisms is needed.

## 5. Conclusion

An extensive experimental campaign was conducted to investigate bubble hydrodynamics and aerosol retention from a submerged nozzle in a shallow pool using the TRISTAN and SAAB facilities, respectively. Conditions were limited to low momentum bubbly flows. Nitrogen was injected through 5 and 10 mm nozzles at flow rates of 1–10 $l_n$/min with 300 mm water submergence. The HSC images revealed aperiodic globule formation with strong coalescence and breakup, particularly at higher flow rates and with the smaller nozzle. Time-averaged GVF and velocity distributions obtained from both HSC and WMS showed that the effect of the nozzle is more evident in the region around the nozzle.

An advanced image-processing approach was developed to analyze globule formation and to characterize the globule properties at the detachment as a function of the Weber number. The results show consistent trends with increasing *We*, but significant differences remain between nozzle sizes. However, applying a scaling factor based on the square root of the nozzle diameter ratio enabled a data collapse around a single curve for both nozzles. This scaling approach was in addition validated using data from the literature. This allowed the derivation of a fit function linking globule diameter to *We* and nozzle size for *We* range up to 70. The same methodology can be extended to other globule characteristics.

The conducted aerosol scrubbing experiments highlighted several trends. Firstly, because of competing effects, particle removal rate is found to be insensitive to injection flow rates. On the other hand, larger particles are more easily scrubbed than smaller one thanks to inertial forces. Finally, under otherwise identical conditions, use of the smaller nozzle results mostly in a slight improvement of aerosol retention.

An exhaustive and reliable database on bubble hydrodynamics and aerosol retention has been established in this work. The next step will involve reporting selected CFD simulations of the hydrodynamics and aerosol retention tests.

## CRediT authorship contribution statement

**Nabil Ghendour:** Writing – original draft, Software, Methodology, Investigation, Formal analysis, Data curation, Conceptualization. **Detlef Suckow:** Writing – review & editing, Supervision, Methodology, Conceptualization. **Abdelouahab Dehbi:** Writing – review & editing, Supervision, Investigation, Conceptualization. **Michael Klauck:** Writing – review & editing, Methodology, Conceptualization.

## Declaration of competing interest

The authors declare that they have no known competing financial interests or personal relationships that could have appeared to influence the work reported in this paper.

## Acknowledgements

The work was performed in the framework of the research collaboration “Experimental studies and CFD simulations of aerosol removal by water pools (Pool scrubbing)“between the Paul Scherrer Institut (PSI), Switzerland and the Forschungszentrum Jülich Gmbh (FZJ) in Germany under the FZJ contract number 42276687 and the PSI quote 2021–00907.

This research collaboration is part of the HECTAR project (“Hydrodynamic Experiments to Characterize Aerosol Retention”) partly funded under contract LRT-20_11 by swissnuclear, the association of the Swiss nuclear power station operators.

The financial support of both organizations is gratefully acknowledged.

## Data availability

Data will be made available on request.

## References

Abe, Yutaka, Fujiwara, Kota, Saito, Shimpei, Yuasa, Tomohisa, Kaneko, Akiko, 2018. Bubble dynamics with aerosol during Pool scrubbing. Nuclear Engineering and Design 337 (May), 96–107. https://doi.org/10.1016/j.nucengdes.2018.06.017.

Bertola, Volfango, 2003. In: Bertola, Volfango (Ed.), 450 *Modelling and Experimentation in Two-Phase Flow*. Springer Vienna, Vienna. https://doi.org/10.1007/978-3-7091-2538-0.

Betschart, Torsten Thomas, 2015. Two-phase flow investigations in large diameter channels and tube bundles. PhD thesis, ETH-Zürich.

Dehbi, A., Cheng, X., Liao, Y., Okagaki, Y., Pellegrini, M., 2022. “A COMPARATIVE CFD EXERCISE ON BUBBLE HYDRODYNAMICS USING EULER-EULER AND INTERFACE TRACKING APPROACHES.” In *NURETH-19*.

Dehbi, A., Suckow, D., Guentay, S., 2001. Aerosol retention in low-subcooling pools under realistic accident conditions. Nuclear Engineering and Design 203 (2–3), 229–241. https://doi.org/10.1016/S0029-5493(00)00343-5.

Diao, Han, Zhou, Yanmin, Haifeng, Gu, Li, Yingzhi, Yan, Chaoxing, 2020. Experimental study on the scrubbing efficiency of aerosols contained in horizontal and vertically downward submerged gas jet. Prog. Nucl. Energy 126 (April), 103406. https://doi.org/10.1016/j.pnucene.2020.103406.

Dong, Shichang, Yang, Jun, 2019. Overview of the experimental studies and numerical simulations on the filtered containment venting systems with wet scrubbers. Annals of Nuclear Energy 132, 461–485. https://doi.org/10.1016/j.anucene.2019.04.042.

Farhat, Mohamad, Chinaud, Maxime, Nerisson, Philippe, Vauquelin, Olivier, 2021. Characterization of bubbles dynamics in aperiodic formation. Int. J. Heat Mass Transf. 180, 121646. https://doi.org/10.1016/j.ijheatmasstransfer.2021.121646.

Farhat, Mohamad, Nerisson, Philippe, Cantrel, Laurent, Chinaud, Maxime, Vauquelin, Olivier, 2023. Hydrodynamic aspects of aerosols Pool scrubbing. Chem. Eng. Res. Des. 191, 646–657. https://doi.org/10.1016/j.cherd.2023.02.004.

Fujiwara, Kota, Kikuchi, Wataru, Nakamura, Yuki, Yuasa, Tomohisa, Saito, Shimpei, Kaneko, Akiko, Abe, Yutaka, 2019. Experimental study of single-bubble behavior containing aerosol during Pool scrubbing. Nucl. Eng. Des. 348 (April), 159–168. https://doi.org/10.1016/j.nucengdes.2019.04.015.

Ghendour, Nabil, Meribout, Mahmoud, Azzi, Abdelwahid, 2020. Review of measurement techniques for void fraction of two-phase flow through annulus. Measurement 165, 108196. https://doi.org/10.1016/j.measurement.2020.108196.

Hur, Young Gul, Yang, Jung Hoon, Jung, Heon, Park, Seung Bin, 2013. Origin of regime transition to turbulent flow in bubble column: orifice- and column-induced transitions. Int. J. Multiphase Flow 50, 89–97. https://doi.org/10.1016/j.ijmultiphaseflow.2012.11.001.

Kim, Yo Han, Kam, Dong Hoon, Yoon, Jongwoong, Jeong, Yong Hoon, 2020. The importance of representative aerosol diameter and bubble size distribution in Pool scrubbing. Ann. Nucl. Energy 147, 107712. https://doi.org/10.1016/j.anucene.2020.107712.

Liu, Liu, Yan, Hongjie, Zhao, Guojian, 2015. Experimental studies on the shape and motion of air bubbles in viscous liquids. Exp. Thermal Fluid Sci. 62, 109–121. https://doi.org/10.1016/j.expthermflusci.2014.11.018.

Maxwell, James Clerk, 1881. A Treatise on Electricity and Magnetism.

Mosdorf, R., Wyszkowski, T., 2011. Experimental investigations of deterministic Chaos appearance in bubbling flow. International Journal of Heat and Mass Transfer 54 (23–24), 5060–5069. https://doi.org/10.1016/j.ijheatmasstransfer.2011.07.023.

Pan, Weitong, Chen, Xueli, Dai, Gance, Wang, Fuchen, 2020. Enhanced effect of bubble deformation on internal particle transport. Ind. Eng. Chem. Res. https://doi.org/10.1021/acs.iecr.9b05158.

Prasser, Horst Michael, Häfeli, Richard, 2018. Signal response of wire-mesh sensors to an idealized bubbly flow. Nuclear Engineering and Design 336, 3–14. https://doi.org/10.1016/j.nucengdes.2017.04.016.

Roth, Bernhard, Suckow, Detlef, Dehbi, Abdel, 2022. "Experimental Study of Pool Scrubbing Related Bubble Hydrodynamics in the Globule Flow Regime." In *NURETH-19*.

Wang, Han-bin, Yang, Xu, Li, Si-ying, Wang, Jin-jun, 2024. Effects of gas flow rate on rising bubble chains and induced flow fields : an experimental study. International Journal of Multiphase Flow 170 (July 2023), 104623. https://doi.org/10.1016/j.ijmultiphaseflow.2023.104623.

Zhang, Wei, Chen, Xueli, Pan, Weitong, Jianliang, Xu., 2022a. Numerical simulation of wake structure and particle entrainment behavior during a single bubble ascent in liquid-solid system. Chem. Eng. Sci. 253, 117573. https://doi.org/10.1016/j.ces.2022.117573.

Zhang, Yixiang, Zhu, Jianlu, Teng, Lin, Li, Yuxing, 2022b. Evaluation and dynamic breakup of bubble size distribution of liquified natural gas release underwater. J. Nat. Gas Sci. Eng. 102 (April), 104600. https://doi.org/10.1016/j.jngse.2022.104600.